International Journal of Heat and Mass Transfer 184 (2022) 122285

Contents lists available at ScienceDirect

International Journal of Heat and Mass Transfer

journal homepage: www.elsevier.com/locate/hmt

Molecular simulation of steady-state evaporation and condensation of water in air

Eric Bird[a], Jesus Gutierrez Plascencia[a], Pawel Keblinski[b], Zhi Liang[a,*]

[a] Department of Mechanical Engineering, California State University, Fresno, CA 93740, USA
[b] Department of Materials Science and Engineering, Rensselaer Polytechnic Institute, Troy, NY 12180, USA

ARTICLE INFO

Article history:
Received 14 September 2021
Revised 21 October 2021
Accepted 18 November 2021
Available online 4 December 2021

Keywords:
Evaporation/condensation
Schrage Equation
Non-condensable gas
Water-air interface
Molecular dynamics

ABSTRACT

It was shown in recent experiments and molecular dynamics (MD) simulations that Schrage equation predicts evaporation and condensation rates of water in the absence of a non-condensable gas with good accuracy. However, it is not clear whether Schrage equation is still accurate or even valid for quantifying water evaporation and condensation rates in air. In this work, we carry out MD simulations to study steady-state evaporation and condensation of water at a planar water-air interface. The simulation results show that the evaporation and condensation fluxes of water in the presence of air are still in a good agreement with the predictions from Schrage equation. From Schrage equation and Stefan's law of mass diffusion, we derive an analytical expression for the effective thermal conductivity of a planar heat pipe. The analytical prediction of the dependence of effective thermal conductivity on heat pipe length and density of non-condensable gas is corroborated by our MD simulation results and recent experimental data.

1. Introduction

Water evaporation/condensation in air is a process of great importance to a variety of natural phenomena [1–4] and engineering applications [5–7]. A fundamental understanding of heat and mass transfer at a water-air interface requires treatment from the kinetic theory of gases (KTG) [8–11]. Two relationships that were derived from the KTG and widely used in the past decades to model evaporation and condensation processes are Hertz-Knudsen (HK) relationships [8–10] and Schrage relationships [11,12]. Both relationships provide an expression that correlates the evaporation/condensation flux with the temperature and density of fluid near a liquid-gas interface and the mass accommodation coefficient (MAC). Despite the wide use of HK and Schrage relationships in analyses of water evaporation and condensation processes, the accuracy and even the validity of these relationships are still a subject of extensive discussion because accurate measurement of the quantities in HK and Schrage relationships remains challenging in experiment [8]. Although recent experimental and molecular dynamics (MD) studies [13,14] suggest that Schrage relationships are capable of predicting evaporation and condensation rates of water in the absence of a non-condensable gas with good accuracy, the validity of Schrage relationships in the prediction of evaporation and condensation rates of water in the presence of air is still debated.

To mitigate the experimental challenges in the investigation of water evaporation and condensation processes, we use MD simulations in this work to test the validity and accuracy of Schrage relationships in quantifying steady-state evaporation/condensation rates of water at a planar water-air interface. MD simulations determine positions, velocities, and forces of all atoms and molecules in a model system by numerical integration of Newton's equation of motion. Therefore, they can readily determine all the quantities in Schrage relationships, including the MAC, and the temperature, density, and macroscopic velocity of model fluids with high fidelity and with high temporal and spatial resolutions that are difficult to achieve experimentally. We have used MD simulations to study evaporation and condensation of monatomic fluids and polymers and showed that Schrage relationships are accurate in the prediction of evaporation and condensation rates of these model fluids [15–19]. MD simulations were also successfully used to understand the evaporation and condensation processes of a pure water, i.e., water in the absence of any non-condensable gases [14,20]. Therefore, MD simulations are a very powerful tool for microscopic analyses of evaporation and condensation processes. In this work, we will add air in the MD model to study evaporation and con-

* Corresponding author.
E-mail address: zliang@csufresno.edu (Z. Liang).

https://doi.org/10.1016/j.ijheatmasstransfer.2021.122285
0017-9310/

Nomenclature

D	self-diffusion coefficient
D_{AB}	binary diffusion coefficient
D_{H_2O-air}	binary diffusion coefficient of water-air gas mixture
$D_{H_2O-N_2}$	binary diffusion coefficient of water-nitrogen gas mixture
f	shifted Maxwell velocity distribution
G	thermal conductance
h_f	enthalpy of saturated liquid
h_{fg}	latent heat of vaporization
h_g	enthalpy of saturated vapor
J	net molar flux across liquid-gas interface at steady state
J_{con}	net condensation flux at right surface from Schrage prediction
$J_{condensing}$	molar flux of vapor molecules condensing on liquid surface
J_{evp}	net evaporation flux at left surface from Schrage prediction
$J_{evaporating}$	molar flux of vapor molecules evaporating from liquid surface
J_{H_2O}	molar flux of water at steady-state evaporation/condensation
J_{N_2}	molar flux of nitrogen at steady-state evaporation/condensation
J_{strike}	molar flux of vapor molecules that strike the liquid surface
J_{theory}	molar flux of water from theory
k_{eff}	effective thermal conductivity
L	separation distance between two liquid-gas interfaces
M	molar mass of vapor molecules
N_A	Avogadro constant
N_{inc}	total number of incident water molecules
N_{ref}	total number of incident molecules that return to gas phase
P	pressure
P_{air}	partial pressure of air
q	heat flux
R	universal gas constant
R_{ec}	total thermal resistance between evaporating and condensing liquid surfaces
R_L	conduction resistance in thin liquid layers of heat pipe
R_W	conduction resistance in solid walls of heat pipe
t	time
Δt	time interval for incident molecules crossing imaginary plane to return to vapor phase
Δt_{avg}	average Δt
Δt_{cut}	cutoff Δt
T	temperature
T_h	temperature of heat source
T_l	temperature of heat sink
T_L	temperature of liquid near liquid-gas interface
$\bar{T}_L$	average temperature of two liquid-gas interfaces
ΔT_L	temperature difference between two liquid-gas interfaces
$T_{L,1}$	temperature at evaporating liquid-gas interface
$T_{L,2}$	temperature at condensing liquid-gas interface
T_v	temperature of vapor near liquid-gas interface
u	internal energy
$\vec{v}_i$	translational velocity of water molecule i
$v_{i,x}$	x-component velocity of water molecules i in central gas region
v_n	average normal velocity of incident vapor molecules crossing imaginary plane
v_R	ratio of $v_{v,0}$to the most probable thermal speed of vapor molecules
$v_{v,0}$	macroscopic velocity of vapor near liquid-gas interface
v_x	molecular velocity component along evaporation direction
V	volume of central gas region
Δx	distance between imaginary plane and liquid-gas interface
x_c	position of condensing interface in x-direction
x_e	position of evaporating interface in x-direction
y_{N_2}	molar fraction of nitrogen

Greek symbols

α	mass accommodation coefficient
ρ_{air}	density of air
ρ_f	density of saturated liquid
ρ_g	density of saturated vapor
ρ_{N_2}	density of nitrogen gas
ρ_{NCG}	density of non-condensable gas
ρ_{tot}	total molar density of gas mixture
ρ_v	density of vapor near liquid-gas interface
$\rho_{v,1}$	density of water vapor near evaporating liquid-gas interface
$\rho_{v,2}$	density of water vapor near condensing liquid-gas interface

densation at a planar water-air interface and test the accuracy of Schrage relationships by comparing their predictions with the evaporation/condensation rates obtained directly from MD simulations.

In the next section, we introduce the theoretical background on Schrage relationships. In Sec. 3 we describe the MD model and the basic properties of the model fluid. In Sec. 4 we present results of the steady-state evaporation/condensation process and test the validity of Schrage relationships in quantifying steady-state evaporation/condensation rates of water in the presence of air. Based on Schrage relationships, we derive an analytical expression for effective thermal conductivity of a planar heat pipe and discuss how the effective thermal conductivity will be affected by air pressure in the heat pipe and length of the heat pipe in Sec. 5. Finally, we close with conclusions.

2. Theory

Schrage relationships were derived from the KTG. The key assumption made in Schrage analysis is that the velocity distribution (VD) of vapor molecules near an evaporating liquid-gas surface follows the shifted Maxwell VD [11]:

$$f(v_x) = \sqrt{\frac{M}{2\pi R T_v}} e^{-\frac{M\left(v_x - v_{v,0}\right)^2}{2RT_v}}, \tag{1}$$

where v_x is the molecular velocity component along the evaporation direction, T_v and $v_{v,0}$ are the temperature and macroscopic velocity of vapor near the liquid-gas interface, respectively, R is the universal gas constant, and M is the molar mass of vapor molecules. Here vapor molecules refer to molecules undergoing phase change at the liquid-gas interface, not the non-condensable gas molecules. Using the VD given by Eq. (1), one can readily obtain the molar flux of vapor molecules that strike the liquid surface

(i.e., flux of vapor molecules with $v_x < 0$):

$$J_{strike} = \rho_v \sqrt{\frac{RT_v}{2\pi M}} \Gamma(v_R), \tag{2}$$

where ρ_v is the density of vapor near the liquid-gas interface and v_R is the ratio of $v_{v,0}$ to the most probable thermal speed of vapor molecules:

$$v_R = \frac{v_{v,0}}{\sqrt{2RT_v/M}}. \tag{3}$$

The function $\Gamma(v_R)$ in Eq. (2) is given by [11,12]:

$$\Gamma(v_R) = e^{-v_R^2} - v_R\sqrt{\pi}[1 - erf(v_R)]. \tag{4}$$

Of those molecules that strike the liquid surface, a fraction, α, will change to liquid. The remaining part of molecules will return to vapor phase without phase change. The fraction α is known as the MAC [8,11,12]. Accordingly, the molar flux of vapor molecules condensing on the liquid surface is

$$J_{\text{condensing}} = \alpha \rho_v \sqrt{\frac{RT_v}{2\pi M}} \Gamma(v_R). \tag{5}$$

Similarly, assuming Maxwell VD of liquid molecules on a stationary liquid-gas interface at a temperature of T_L, the molar flux of liquid molecules evaporating from the interface is [21,22]

$$J_{\text{evaporating}} = \alpha \rho_g(T_L) \sqrt{\frac{RT_L}{2\pi M}}. \tag{6}$$

where $\rho_g(T_L)$ is the saturated vapor density at T_L. The net molar flux across the liquid-gas interface is equal to the difference between $J_{\text{evaporating}}$ and $J_{\text{condensing}}$:

$$J = \alpha \sqrt{\frac{R}{2\pi M}} \left(\rho_g(T_L)\sqrt{T_L} - \Gamma(v_R)\rho_v\sqrt{T_v} \right). \tag{7}$$

Eq. (7), which is known as Schrage equation, predicts the evaporation/condensation flux J across a liquid-gas interface at a temperature of T_L when the temperature and density of vapor near the liquid surface are T_v and ρ_v, respectively. If J is greater than 0, net evaporation occurs. If J is less than 0, net condensation occurs. In a steady-state evaporation/condensation process, the net molar flux across a liquid-gas interface equals to the molar flux in the evaporating/condensing vapor. Accordingly, we have

$$J = \rho_v v_{v,0}. \tag{8}$$

Substituting Eq. (8) into Eq. (7), we obtain an implicit equation for $v_{v,0}$ since v_R on the right side of Eq. (7) also depends on $v_{v,0}$. Therefore, once the quantities α, T_L, T_v and ρ_v in Schrage equation are known, one needs to use an iterative procedure to determine $v_{v,0}$, i.e., the macroscopic velocity of the evaporating/condensing vapor flow, and the evaporation/condensation flux J from Eqs. (7) and (8).

One of the advantages of MD simulations is that all quantities in Schrage equation can be determined with high fidelity from MD simulations. This allows us to test the accuracy of the Schrage equation in the prediction of evaporation/condensation flux at different driving force conditions. Moreover, MD simulations allow us to directly measure the VD of evaporating/condensing vapor molecules to validate the key assumption, i.e., Eq. (1), in the Schrage analysis. In this work, we will carry out MD simulations to investigate if the assumption of the shifted Maxwell distribution is still valid for water vapor molecules near an evaporating/condensing water-air interface and test the accuracy of Schrage equation in the prediction of evaporation and condensation rates of water in air.

3. MD simulation of water evaporation and condensation in air

3.1. The MD model

Using MD simulations, we study evaporation/condensation across a planar water-air interface. As depicted in Fig. 1, a representative model system consists of a model fluid mixture confined by two solid Au plates. Each Au plate is formed by a three-layered FCC (100) plane solid Au with a cross section area of 14.7 nm by 14.7 nm. On each of the two inner surfaces of Au plates, we place a liquid water thin film. The initial thickness of the liquid film on the left and right solid surfaces are approximately 5.3 nm and 5.0 nm, respectively, such that the liquid layers are thick enough to avoid effects of disjoining pressure on the equilibrium properties of the model water [14]. The separation between two liquid surfaces is about 300 nm. We approximate air as a N_2 gas and add N_2 molecules between two liquid surfaces. The total number of H_2O molecules and Au atoms are 67280 and 15552, respectively. We will vary the number of N_2 molecules in the gas phase to study effects of N_2 gas concentration on evaporation and condensation rates of water. In MD simulations, periodic boundary conditions (PBCs) are applied in the y and z directions, and atoms in the outermost Au layers are fixed. The fluid in the region from x = 10 nm to x = 300 nm is always in gaseous state in MD simulations. Therefore, we define this region as the central gas region of the model system.

In the MD model, we use a rigid extended simple point charge (SPC/E) model [23] to describe the intermolecular potential of water molecules. The Coulombic interactions in the SPC/E potential are treated by the Wolf summation [24] with a damping factor of 0.15 $Å^{-1}$ and cutoff distance of 9.0 Å. The Wolf summation technique has been shown to produce reasonable saturated densities for SPC/E water [25]. The Lennard-Jones (LJ) potential, with parameters $\sigma = 3.3078$ Å and $\epsilon/k_B = 36.67$ K [26], is used to describe the non-bonded N-N interactions between the N_2 molecules whose bond length is fixed at 1.10 Å [27]. The LJ potential is also used to describe the interactions between N_2 and H_2O molecules with potential parameters determined from the Lorentz-Berthelot mixing rule [28]. In our recent work [29], we used the same potential model to study the coalescence dynamics of N_2 nanobubbles in water. In this work, we will use this model to study water evaporation and condensation in a N_2 gas.

For Au-Au interactions, we use the embedded-atom-method (EAM) potential [30]. The non-bonded interactions between Au and H_2O molecules, and between Au and N_2 molecules are described by the LJ potential with parameters taken from universal force field (UFF) [31] and calculated by the LB mixing rule. The cutoff distance for all LJ interactions in the MD model is 9.0 Å. In MD simulations, a velocity Verlet algorithm is used to integrate the equations of translational motions [28]. A leapfrog algorithm for quaternions developed by Omelyan [32] is used for integration of the equations of rotational motions. A time step size of 1 fs is used in all MD simulations.

3.2. The fluid properties of the model water

To determine the evaporation/condensation flux from Schrage equation, i.e., Eq. (7), we need to know the accurate value of α and ρ_g of the model water. Therefore, we use equilibrium MD (EMD) simulations described in Sec. 3.2.1 and Sec. 3.2.2 to first determine the saturated vapor density, ρ_g, and the MAC, α of the model water as a function of temperature.

3.2.1. Determination of ρ_g

To determine the ρ_g of the model water, we place a liquid slab of 54000 H_2O molecules in the middle of a simulation box, which

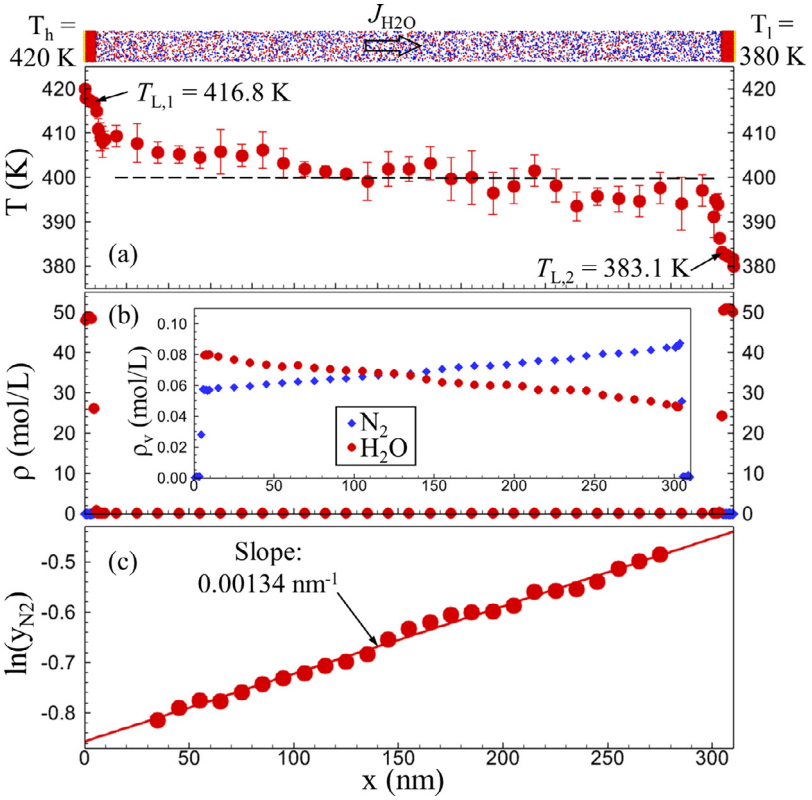

Fig. 1. (Top panel) A snapshot of the model system during NEMD simulation in the representative case of T_h = 420 K, T_l = 380 K, and the average ρ_{N2} = 0.07 *mol/L*. The yellow, red, white, and blue dots in the snapshot represent Au, O, H, and N atoms, respectively (Same in other figures). (Bottom panels) Steady-state (a) temperature, and (b) density profiles in the whole model system, and (c) $\ln(y_{N2})$ profile in the gas region. The inset in (b) shows the density profile in the gas region. The horizontal dashed line in (a) indicates the average temperature in the gas region. The solid line in (c) shows a linear fit to the MD data (For interpretation of the references to color in this figure legend, the reader is referred to the web version of this article).

has a length of 20 nm and cross section area of 14.7 nm by 14.7 nm as shown in Fig. 2. 89 N_2 molecules are added to the gas phase of the simulation box such that the N_2 density in the gas phase is close to the maximum N_2 gas density in subsequent non-equilibrium MD (NEMD) simulations of evaporation and condensation processes. The box size is fixed during the EMD simulation and PBCs are applied in all three directions. We equilibrate the system at multiple temperatures varying from 350 K to 500 K using the Berendsen thermostat [33]. At each temperature, 2 ns is used to equilibrate the system and another 2 ns is used for data averaging. After the model system reaches thermal equilibrium at each temperature, a liquid water slab sandwiched by a gas mixture of N_2 and saturated water vapor is present in the simulation box. The saturated vapor density, ρ_g, and the saturated liquid density, ρ_f, are calculated from the average H_2O density in the gas phase and in the liquid phase, respectively. Figure 2 shows the representative EMD simulation results at $T = 400$ K. If we define the liquid-gas interfacial layer as the region whose density ranges from $\rho_g + 0.01\rho_f$ to $0.95\rho_f$, the result in Fig. 2 shows the thickness of the interfacial layer at $T = 400$ K is $\sim$ 1.5 nm.

In Fig. 3, we show the temperature-dependent ρ_g determined from our EMD simulations has a reasonable agreement with the experimental data [34,35]. We also perform similar EMD simulations in model systems with lower and zero N_2 density and find ρ_g is almost unaffected by the N_2 density. In subsequent NEMD simulations, we study evaporation and condensation of the model water around 400 K. To further verify that our EMD model determines reliable ρ_g for the model water around 400 K, we compare the simulation results near 400 K to the prediction from the Clausius-Clapeyron equation [36]. If the ideal gas assumption is valid for the saturated vapor of the model water, the temperature-dependent ρ_g satisfies [36]:

$$\frac{d(\ln \rho_g)}{d(1/T)} = -\frac{h_{fg}}{R} + T, \tag{9}$$

where h_{fg} is the latent heat at a given temperature T. To find h_{fg} of the model water at a temperature of 400 K, we carry out separate EMD simulations to determine the internal energy, u, and pressure, P, of the saturated liquid water and the saturated vapor water at $T = 400$ K. Using the u, P, and ρ_g obtained from EMD simulations, we determine the enthalpy, h_f, of the saturated liquid and the enthalpy, h_g, of the saturated vapor. The difference between the two enthalpies gives $h_{fg} = 40.77$ *kJ/mol* for the model water at $T = 400$ K which agrees reasonably with the experimental value $h_{fg} = 39.32$ *kJ/mol* [34,35].

To investigate if the temperature-dependent ρ_g satisfies Eq. (9), we take five MD data points ranging from 375 K to 425 K and fit $\ln(\rho_g)$ vs. $1/T$ data with a linear function. As shown in the inset of Fig. 3, the linear fit gives a slope of -5054 K at $T = 400$ K, which has a reasonable agreement with -4504 K predicted by Eq. (9). Using the calculated P and ρ_g of the saturated model water vapor at $T = 400$ K, we find the compressibility factor (CF) of the saturated vapor is 0.93, which implies the saturated vapor of model water is close to, but not a perfect ideal gas at $T = 400$ K. In our recent study on the phase change of a model n-dodecane at $T = 450$ K [19], we also found that the CF of the saturated vapor n-dodecane is 0.93 and the slope of $\ln(\rho_g)$ vs. $1/T$ deviates $\sim$ 10% from the prediction from Eq. (9). Therefore, we believe the 10% difference between the MD result and the theoretical prediction is caused by the non-ideal gas behavior of the model water vapor around

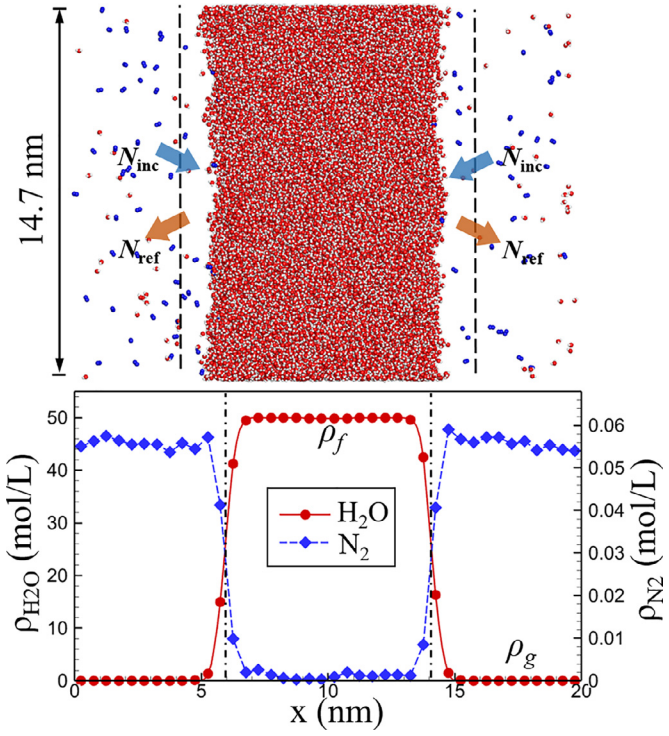

Fig. 2. A snapshot of a liquid water slab sandwiched by a gas mixture of N_2 and saturated water vapor at a temperature of 400 K, and the corresponding density profile in the model fluid system. The dash-dot lines indicate the position of liquid-gas interfaces. The vertical dashed lines in the snapshot indicate the position of imaginary planes used for determination of the MAC. The solid and dashed lines in the density profile is used to guide the eye.

$T = 400$ K, and our temperature-dependent ρ_g data are reliable in the analysis of the subsequent NEMD simulation results of evaporation and condensation processes.

3.2.2. Determination of α

Using the same EMD model described in Sec. 3.2.1, we determine the MAC which is defined as the fraction of vapor molecules that strike the liquid surface and are accommodated to the liquid phase. To determine if an incident vapor molecule is accommodated to or reflected from the liquid surface, we set an imaginary plane 2 nm from the liquid-gas interface as shown in Fig. 2. The liquid-gas interface is defined at the position where the water density equals to $(\rho_g+\rho_f)/2$. We define vapor molecules that cross the imaginary plane and move towards the interface as incident molecules. The distance between the imaginary plane and the interface is greater than the thickness ($\sim$ 1.5 nm) of the liquid-gas interfacial layer to ensure that the vapor molecules that cross the imaginary plane are out of the interface. This distance should also be much smaller than the mean free path (MFP) of vapor molecules to ensure that the incident molecules mainly collide with the liquid surface, not with other vapor molecules.

To estimate the MFP of saturated vapor of model water, we carry out a separate EMD simulation in a cubic simulation box containing saturated water vapor at $T = 400$ K. Using the EMD simulation, we obtain the self-diffusion coefficient $D = 1.3 \times 10^{-5}\ m^2/s$ for the model water vapor from Green-Kubo formula [28]:

$$D = \frac{1}{3}\int_0^\infty dt\langle \vec{v}_i(t)\cdot\vec{v}_i(0)\rangle, \tag{10}$$

where $\vec{v}_i$ is the translational velocity of water molecule i, and t is time. Substituting this value into the Einstein-Smoluchowski's equation [37], we find the molecular MFP in the saturated model water vapor at $T = 400$ K is about 38 nm, which is much greater than the distance between the imaginary plane and the interface.

To determine the MAC from the model system shown in Fig. 2, we follow the trajectory of each incident vapor molecule to determine the time interval, Δt, for each incident molecule to cross the imaginary plane again and return to the vapor phase. The time interval, Δt, for vapor molecules that are directly reflected by the liquid surface should be smaller than that for vapor molecules that are first accommodated to the liquid phase and later evaporated. Therefore, we need to find a cutoff time interval, Δt_{cut}, to determine if the incident molecule is accommodated to the liquid surface. Near a liquid-gas interface in thermal equilibrium, the average normal velocity of incident vapor molecules crossing an imaginary plane is $v_n = \sqrt{\pi RT/2M}$ according to the KTG [38]. For vapor water at $T = 400$ K, the KTG predicts $v_n = 539\ m/s$ which agrees well with $v_n = 536\pm9\ m/s$ directly obtained from our EMD simulations. Accordingly, for incident molecules that are directly reflected by the interface, the average time flight time should be $\Delta t_{avg} = 2\Delta x/v_n = 7.4\ ps$, where $\Delta x = 2$ nm is the distance between the imaginary plane and the liquid-gas interface. Hence, we use $\Delta t_{cut} = 7.4\ ps$ to determine the MAC of the model water at $T = 400$ K. For MACs at other temperatures, we use the Δt_{cut} corresponding to the average flight time at the given temperature to evaluate the corresponding MAC.

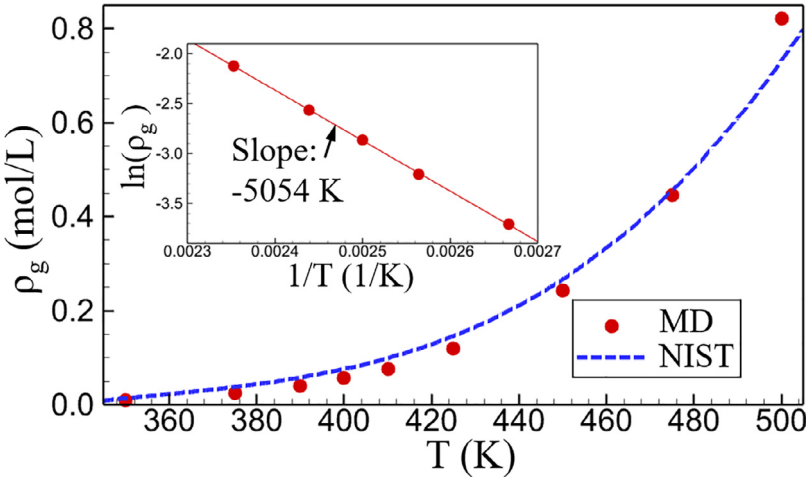

Fig. 3. The saturated vapor density, ρ_g, of model water as a function of temperature. The dashed line is the experimental data taken from NIST [34,35]. The inset shows the linear fit to $\ln(\rho_g)$ vs. $1/T$ of the model water in the range from T = 375 K to T = 425 K. The equation of the solid line in the inset is $\ln(\rho_g) = 9.763 - 5054/T$.

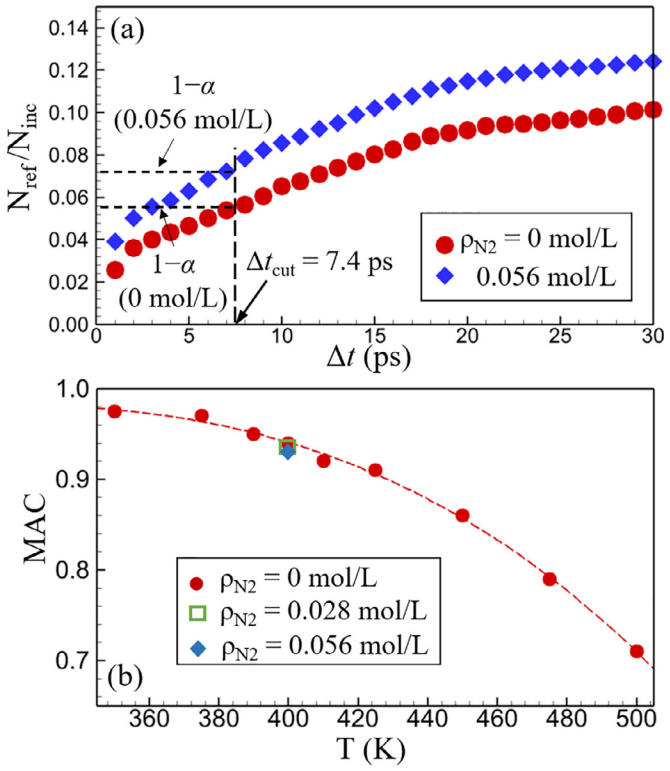

Fig. 4. (a) The ratio of number of molecules returned to vapor within Δt to number of incident vapor molecules at a temperature of 400 K. 1 – N_{ref}/N_{inc} at Δt = 7.4 ps is used to evaluate the MAC. (b) The MD simulation results of the MAC as a function of temperature for the model water. The dashed line in (b) is a third order polynomial fit to the MAC vs. T in this work.

Table 1
The self-diffusion coefficient, D, molecular MFP, compressibility factor, CF, and density, ρ_g, of the model saturated water vapor, and the latent heat, h_{fg}, the MAC, α, of the model water at T = 400 K.

D (m^2/s)	MFP (nm)	h_{fg} (kJ/mol)	α	CF	ρ_g (mol/L)
1.3×10^{-5}	38	40.77	0.94±0.01	0.93	0.058±0.002

In a 2-ns-long EMD run at T = 400 K, we measure the total number of incident water molecules, N_{inc}, and the total number of incident molecules that return to the gas phase, N_{ref}, within Δt. If an incident vapor molecule takes more than Δt_{cut} = 7.4 ps to return to the vapor phase, we consider that the vapor molecule is first accommodated to the liquid and later evaporated. Accordingly, we use $\alpha = 1 - N_{ref}/N_{inc}$ at Δt_{cut} = 7.4 ps to evaluate the MAC at T = 400 K as shown in Fig. 4(a). A similar method has been used in the previous work to evaluate the MAC of monatomic fluids, polymers, and water [14–19]. In the range of N_2 density studied in this work, our MD results show the MAC of the model water depends weakly on the N_2 density (α = 0.93±0.01 for ρ_{N2} = 0.056 mol/L and α = 0.94±0.01 for ρ_{N2} = 0 mol/L). Therefore, we use a pure water system (i.e., ρ_{N2} = 0 mol/L) to determine the temperature-dependent MAC as shown in Fig. 4(b) and assume the MAC is not affected by the N_2 density in the subsequent theoretical analysis of evaporation and condensation processes. Our MD simulation results are consistent with the previous MD studies [14,39] on the MAC of SPC/E water, which show the MAC is around 0.9 at T = 400 K and the MAC decreases with increasing temperature. For the convenience of discussions of simulation results in the following sections, we summarize the properties of the model water at T = 400 K obtained in this section in Tab. 1.

4. NEMD simulation of evaporation and condensation

4.1. NEMD simulation details

To study evaporation and condensation of the water in the model system shown in Fig. 1, we set the left Au plate as a heat source, and the right Au plate as a heat sink. This results in evaporation of water on the left surface and condensation of water on the right surface. The heat source temperature, T_h, and the heat sink temperature, T_l, are maintained in the subsequent MD simulations by velocity rescaling at each time step. T_h and T_l are higher and lower than 400 K by the same amount, respectively, so that the average temperature of the whole model system is around 400 K in all cases. Each heat source-sink simulation run is first performed for 3 ns to allow the system to reach quasi-steady-state evaporation and condensation, which means the evaporation/condensation flux becomes essentially time-independent after 3 ns. Subsequently, the NEMD simulation is carried out for an additional 2 ns for data collection and averaging. We consider the simulated process as a quasi-steady-state evaporation and condensation process because the two liquid-gas interfaces move at a low speed of ∼ 0.1 m/s and during the 2-ns data collection period the interfaces only displace by ∼ 2 Å. In Sec. 3, we find the MFP of the saturated model water vapor is about 38 nm. When N_2 gas is added between two interfaces separated by 300 nm, the MFP of vapor molecules will be smaller. Hence, the Knudsen number in the gas phase of the model system is less than 0.12.

To calculate the steady-state temperature and density profiles, we evenly divide the fluid region less than 10 nm from each of the two solid surfaces into ten bins. The 1-nm bin width in this region allows us to find the location and temperature of the liquid surface with precision. In the 290-nm-long central gas region, we evenly divide the region into 29 bins. The 10-nm bin width in the central gas region allows us to obtain good statistics of gas properties. The steady-state evaporation/condensation molar flux is determined by $J = \Sigma v_{i,x}/(VN_A)$, where N_A is the Avogadro constant, V and $v_{i,x}$ are the volume and the x-component velocity of water molecules in the central gas region, respectively. The contribution from the macroscopic velocity is subtracted in the calculation of temperature in each bin. To further improve the accuracy of the simulation results, four independent runs are performed in each case of MD simulations. The uncertainties of the simulation results are determined by analyses of these independent runs.

4.2. Representative simulation results

The representative NEMD simulation results in the case of T_h = 420 K, T_l = 380 K, and the average ρ_{N2} = 0.07 mol/L are shown in Fig. 1. There are two heat transfer modes between the two liquid-gas interfaces. One is the bulk motion of water vapor caused by evaporation and condensation at the two interfaces. The other is heat conduction since a temperature gradient in the gas phase is observed in Fig. 1(a). As a comparison, Fig. 5(a) shows the temperature gradient in the gas phase is almost zero if there is no N_2 gas in the model system, indicating that the heat conduction in Fig. 1(a) is mainly due to the presence of non-condensable N_2 gas. Although heat conduction occurs in the gas phase, the heat conduction flux is negligible compared to the evaporation/condensation heat flux. Furthermore, Fig. 1(a) shows the temperature in the gas phase generally falls within 400±5 K. A ∼ 1% change of T_v in Schrage equation, i.e., Eq. (7), can only result in a small error in the prediction of the evaporation/condensation flux. Therefore, we will approximate the T_v in Schrage equation as the average gas temperature in the model system in the subsequent analysis of the evaporation and condensation process.

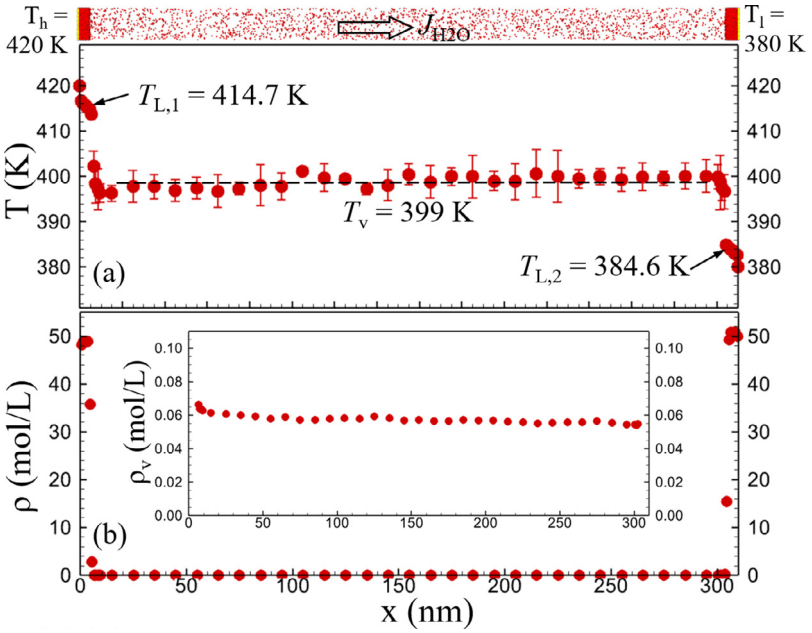

Fig. 5. (Top panel) A snapshot of the model system during NEMD simulation in the case of T_h = 420 K, T_l = 380 K, and ρ_{N2} = 0 *mol/L*. (Bottom panels) Steady-state (a) temperature, and (b) density profiles. The inset in (b) shows the density profile in the gas region. The horizontal dashed line in (a) indicates the average temperature in the gas region.

There are also two mass transfer modes between the two liquid-gas interfaces. One is the mass transfer by bulk motion of the gas mixture. The other is the diffusive mass transfer since an evident density gradient of water vapor is observed in the gas phase as shown in Fig. 1(b). From the NEMD simulation, we directly obtain the steady-state evaporation/condensation flux J_{H2O} = 0.50±0.03 *mol/cm*^{2}*·s* and $J_{N2} \approx 0$ *mol/cm*^{2}*·s*. Hence, the mass diffusion in the gas region is the diffusion of water vapor through a stagnant N_2 gas, which is a typical Stefan flow [38]. As a comparison, Fig. 5(b) shows the density gradient in the gas phase is almost zero when there is no N_2 gas in the model system, indicating that the mass transfer is dominated by mass convection in the absence of non-condensable N_2 gas.

To compare J_{H2O} with the prediction from Schrage equation, we first find the temperature at the evaporating liquid-gas interface $T_{L,1}$ = 416.8 K and at the condensing interface $T_{L,2}$ = 383.1 K as shown in Fig. 1(a). Using the ρ_g vs. T data found in Sec. 3.2.1, we obtain $\rho_g(T_{L,1})$ = 0.095 *mol/L* and $\rho_g(T_{L,2})$ = 0.033 *mol/L*. Furthermore, using the α vs. T data obtained in Sec. 3.2.2, we obtain $\alpha(T_{L,1})$ = 0.91 and $\alpha(T_{L,2})$ = 0.95. Additionally, we find the water vapor density near the evaporating interface $\rho_{v,1}$ = 0.078 *mol/L* and near the condensing interface $\rho_{v,2}$ = 0.048 *mol/L*. $\rho_{v,1}$ and $\rho_{v,2}$ are obtained in the leftmost bin and the rightmost bin of the central gas region, respectively. All these properties are summarized in Tab. 2. Using the above properties and the average gas temperature T_v = 400 K, Schrage equation predicts the net evaporation flux at the left surface J_{evp} = 0.52 *mol/cm*^{2}*·s* and the net condensation flux at the right surface J_{con} = 0.53 *mol/cm*^{2}*·s*, respectively. Both theoretical predictions agree with the MD simulation result J_{H2O} = 0.50±0.03 *mol/cm*^{2}*·s* very well.

The accurate prediction from Schrage equation implies the key assumption regarding the VD of vapor molecules near an evaporating/condensing surface in Schrage analysis is still valid in the case of water evaporation/condensation in a non-condensable gas. To directly verify this assumption, we measure the VD of water vapor molecules in the leftmost (i.e., closest to the evaporating surface) and rightmost (i.e., closest to the condensing surface) bins of the central gas region from MD simulations. Using J_{H2O} = 0.50 *mol/cm*^{2}*·s*, $\rho_{v,1}$ = 0.078 *mol/L* and $\rho_{v,2}$ = 0.048 *mol/L*, we obtain the macroscopic vapor velocity $v_{v,0}$ near the evaporating and the condensing surfaces are 64 m/s and 104 m/s, respectively. Substituting $v_{v,0}$ and T_v = 400 K into Eq. (1), we obtain the shifted Maxwell VD (SMVD) assumed in Schrage analysis. Fig. 6 shows the VDs obtained directly from the MD simulation closely follow the SMVD given by Eq. (1). Hence, the MD results verify the key assumption in Schrage analysis.

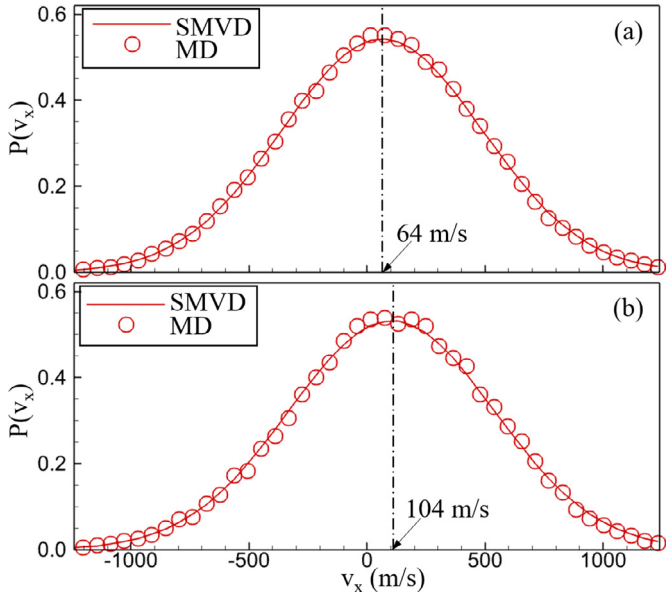

Fig. 6. The steady-state x-component VD of water vapor molecules in the (a) leftmost bin (closet to the evaporating surface), and (b) rightmost bin (closest to the condensing surface) of the central gas region in the representative case of T_h = 420 K, T_l = 380 K, and ρ_{N2} = 0.07 *mol/L*. The scatters are VDs obtained directly from MD simulations. The lines are the SMVD given by Eq. (1) with T_v = 400 K. The vertical dash-dot lines show the mean velocity of vapor molecules.

Table 2
Comparison of the molar fluxes J_{H2O} obtained from NEMD simulations with the predictions from the Schrage relationships. J_{evp} and J_{con} are evaporation and condensation molar fluxes predicted by Schrage relationships, respectively. Error% is defined as $|J_{theory}-J_{H2O}|/J_{H2O}$. The uncertainties of $T_{L,1}$ and $T_{L,2}$ are less than 0.1 K. The uncertainties of $\rho_{v,1}$ and $\rho_{v,2}$ are less than 0.002 *mol/L*. The uncertainties of J_{H2O} are less than 0.03 mol/cm^2s.

T_h	T_l	$T_{L,1}$	$T_{L,2}$	ρ_{N2}	$\rho_{v,1}$	$\rho_{v,2}$	$\rho_{tot}D_{H2O\text{-}N2}$	J_{H2O}	J_{evp}	J_{con}	Error%	
(K)		(K)			(*mol/L*)		(*mol/m·s*)	(mol/cm^2s)			Evp.	Con.
420.0	380.0	414.7	384.6	0.000	0.061	0.056	-	0.76	0.77	0.80	1.3	5.3
412.5	387.5	409.1	390.0	0.000	0.058	0.054	-	0.47	0.49	0.45	4.2	4.2
420.0	380.0	415.7	383.7	0.035	0.070	0.051	0.0036	0.60	0.62	0.65	3.3	8.3
412.5	387.5	409.5	389.6	0.035	0.064	0.052	0.0037	0.37	0.36	0.38	2.7	2.7
420.0	380.0	416.8	383.1	0.070	0.078	0.048	0.0040	0.50	0.52	0.53	4.0	6.0
412.5	387.5	409.9	389.1	0.070	0.067	0.050	0.0040	0.32	0.30	0.35	6.3	9.4

4.3. Effects of ρ_{N2} on J

To study the effects of ρ_{N2} on evaporation and condensation rates of water in the model system, we set $\rho_{N2} = 0$ *mol/L*, 0.035 *mol/L*, and 0.07 *mol/L*. The driving force for the evaporation and condensation processes in the model system is the temperature difference, $\Delta T_L = T_{L,1} - T_{L,2}$, between the two liquid-gas interfaces. For each ρ_{N2}, we carry out NEMD simulations under two temperature-difference conditions: (1) $T_h = 420$ K, $T_l = 380$ K and (2) $T_h = 412.5$ K, $T_l = 387.5$ K. It is shown in Tab. 2 that the average of the two liquid-gas interface temperatures, $\bar{T}_L = (T_{L,1} + T_{L,2})/2$, is close to 400 K in all cases and the evaporation/condensation molar flux, J_{H2O}, obtained from MD simulations increases with ΔT_L and decreases with ρ_{N2}. In all simulated cases, the predictions from Schrage equation deviate less than 10% from the MD results J_{H2O}.

Since our MD simulation results show Schrage equation is accurate in the prediction of evaporation and condensation flux of the model water, we will use analytical relationships derived from Schrage equation to quantitatively understand the dependence of J_{H2O} on ρ_{N2} and ΔT_L found in our MD simulations. First, when $\rho_{N2} = 0$, Fig. 5 shows that the temperature and density in the gas region are almost constant. Accordingly, in the limit of $\Delta T_L/\bar{T}_L \ll 1$, which is the case for our modeling results, one can obtain the following relationship from Schrage equation [15,19]

$$\left(\frac{J}{\Delta T_L}\right)_0 \approx \frac{\alpha(\bar{T}_L)}{2-\alpha(\bar{T}_L)}\sqrt{\frac{R}{2\pi M\bar{T}_L}}\rho_g(\bar{T}_L)\left(\frac{\bar{T}_L}{\rho_g(\bar{T}_L)}\frac{d\rho_g}{dT}\bigg|_{\bar{T}_L}+\frac{1}{2}\right), \tag{11}$$

The subscript 0 on the left side of Eq. (11) indicates the relationship is for a pure water system, i.e., $\rho_{N2} = 0$. If the water vapor can be approximated as an ideal gas, one can use the Clausius–Clapeyron equation (i.e., Eq. (9)) to further reduce Eq. (11) to [15,19]

$$\left(\frac{J}{\Delta T_L}\right)_0 \approx \frac{\alpha(\bar{T}_L)}{2-\alpha(\bar{T}_L)}\sqrt{\frac{R}{2\pi M\bar{T}_L}}\rho_g(\bar{T}_L)\left(\frac{h_{fg}(\bar{T}_L)}{R\bar{T}_L}-\frac{1}{2}\right), \tag{12}$$

Note that all properties on the right side of Eq. (12) are evaluated at $\bar{T}_L$. This indicates that the evaporation/condensation flux in the model system will be proportional to ΔT_L if $\bar{T}_L$ remains constant. It is shown in Tab. 3 and Fig. 7 that in the case of $\rho_{N2} = 0$, $\bar{T}_L = 399.6\pm0.1$ K and J_{H2O} obtained from MD simulations is proportional to ΔT_L with a slope of 0.025 $mol/cm^2{\cdot}s{\cdot}K$. Using α, ρ_g, and h_{fg} obtained in Sec. 3, Eq. (12) predicts $J/\Delta T_L = 0.025$ $mol/cm^2{\cdot}s{\cdot}K$, which is in excellent agreement with the slope found in Fig. 7.

To correlate the slope $J/\Delta T_L$ with ρ_{N2}, we must consider the mass diffusion in the gas mixture in addition to the evaporation and condensation processes at the two interfaces because of the evident density gradient observed in the gas mixture. In Sec. 4.2,

Table 3
Comparison of $J/\Delta T_L$ obtained directly from MD simulations to the prediction from Eq. (15). $\rho_{tot}D_{H2O\text{-}N2} = 3.85 \times 10^{-3}$ *mol/m·s* and $L = 300$ nm are used in the theoretical prediction.

ρ_{N2} (*mol/L*)	$\bar{T}_L$ (K)	$J/\Delta T_L$ ($mol/cm^2s{\cdot}K$)	
		MD	Theory
0	399.6	0.025	0.025
0.035	399.6	0.019	0.018
0.070	399.7	0.015	0.014

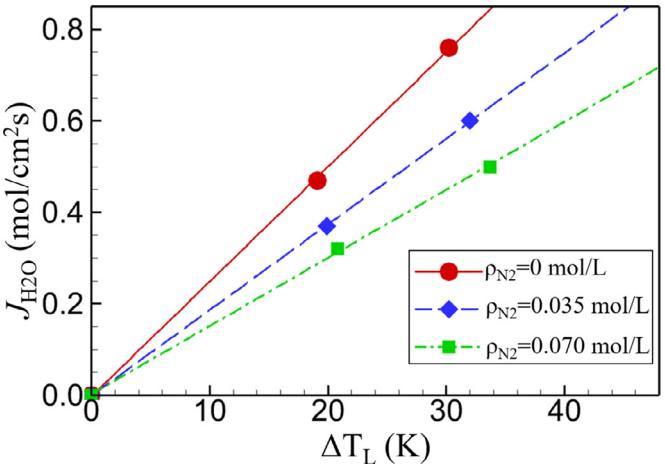

Fig. 7. Steady-state evaporation/condensation flux of water as a function of ΔT_L obtained from NEMD simulations. The dashed line shows the linear fit to J_{H2O} vs. ΔT_L. The uncertainty of J_{H2O} is smaller than the size of symbols.

we showed the mass flow in the H_2O-N_2 gas mixture is a Stefan flow. Hence, J_{H2O} can be also determined by Stefan's law [40]:

$$J_{H_2O} = \frac{\rho_{tot}D_{H_2O-N_2}}{L}\ln\frac{y_{N_2}(x_c)}{y_{N_2}(x_e)}, \tag{13}$$

where ρ_{tot} is the total molar density of the gas mixture, which is essentially a constant in the gas phase, $D_{H2O\text{-}N2}$ is the binary diffusion coefficient, x_e and x_c are the position of evaporating and condensing interfaces, respectively, L is the separation between two liquid-gas interfaces, and y_{N2} is the molar fraction of N_2 ($y_{N2} = \rho_{N2}/\rho_{tot}$). In Sec. 3, we showed the model fluid is close to an ideal gas. The KTG predicts that the diffusion coefficient $D_{H2O\text{-}N2}$ of an ideal gas is independent of the composition ratio and is inversely proportional to ρ_{tot} at a given temperature. Since the gas temperature in all simulation cases is close to 400 K, the product $\rho_{tot}D_{H2O\text{-}N2}$ should be approximately a constant. To verify this KTG prediction, we calculate $\rho_{tot}D_{H2O\text{-}N2}$ of the model fluid from the

following relationship derived from Eq. (13):

$$\ln y_{N_2}(x) = \ln y_{N_2}(x_e) + \frac{J_{H_2O}}{\rho_{tot} D_{H_2O-N_2}} x. \tag{14}$$

Consistent with the prediction of Eq. (14), Fig. 1(c) shows $\ln(y_{N2})$ is indeed a linear function of x. A linear fit to the MD data in Fig. 1(c) gives the slope $J_{H2O}/\rho_{tot}D_{H2O\text{-}N2} = 0.00134\ nm^{-1}$. Using $J_{H2O} = 0.50\ mol/cm^2{\cdot}s$, we obtain $\rho_{tot}D_{H2O\text{-}N2} = 3.7 \times 10^{-3}\ mol/m{\cdot}s$. Using a similar method, we find $\rho_{tot}D_{H2O\text{-}N2}$ in other simulation cases. As shown in Tab. 3, the calculated $\rho_{tot}D_{H2O\text{-}N2}$ all fall within $0.0038\pm0.0002\ mol/m{\cdot}s$, which means $\rho_{tot}D_{H2O\text{-}N2}$ is almost a constant as expected. Therefore, we use the average value $\rho_{tot}D_{H2O\text{-}N2} = 0.00385\ mol/m{\cdot}s$ in the following calculations.

From Schrage equation (Eq. (7)) and Stefan's law (Eq. (13)), our previous work [16] derived the following equation to correlate $J/\Delta T_L$ with the density of non-condensable gas (N_2 gas in our model system):

$$\frac{J}{\Delta T_L} = \frac{(J/\Delta T_L)_0}{1 + \frac{\alpha(\bar{T}_L)}{2-\alpha(\bar{T}_L)}\sqrt{\frac{R\bar{T}_L}{2\pi M}}\frac{L\rho_{N_2}}{\rho_{tot}D_{H_2O-N_2}}}, \tag{15}$$

where we approximate the N_2 density at the center of the gas region as the average N_2 gas density ρ_{N2} and approximate the average gas temperature as $\bar{T}_L$. Both approximations are good for our model systems. Since $\bar{T}_L$ and $\rho_{tot}D_{H2O\text{-}N2}$ are both constant in our simulation cases, Eq. (15) predicts that J is proportional to ΔT_L for a given ρ_{N2}, and $J/\Delta T_L$ will decrease with increasing ρ_{N2}. As shown in Tab. 3 and Fig. 7, the slope $J/\Delta T_L$ obtained directly from the MD data agrees with the prediction from Eq. (15) very well for both $\rho_{N2} = 0.035\ mol/L$ and $\rho_{N2} = 0.07\ mol/L$ cases.

5. Effective thermal conductivity of a heat pipe

The model system shown in Fig. 1, which contains a thin liquid water layer on each of the evaporator surface and the condenser surface, is similar to a planar heat pipe. The driving force for the evaporation and condensation in the heat pipe is the temperature difference ΔT_L. Using the analytical equation for $J/\Delta T_L$, i.e., Eq. (15), we can determine the effective thermal conductivity of a planar heat pipe. The temperature difference ΔT_L between the evaporating and condensing liquid surfaces in the heat pipe results in a heat flux $q = Jh_{fg}$ from the evaporator to the condenser of the heat pipe. Accordingly, the thermal conductance between the two liquid surfaces is

$$G = q/\Delta T_L = (J/\Delta T_L)h_{fg}. \tag{16}$$

The thermal conductance is related to the effective thermal conductivity k_{eff} by

$$G = k_{eff}/L, \tag{17}$$

where L is the separation between the evaporating and condensing liquid surfaces. From Eqs. (16) and (17), we obtain the relation between k_{eff} and $J/\Delta T_L$:

$$k_{eff} = (J/\Delta T_L)h_{fg}L. \tag{18}$$

Substituting Eq. (15) into Eq. (18), we obtain the analytical equation to determine k_{eff} as a function of temperature $\bar{T}_L$, density of non-condensable gas (NCG) ρ_{NCG} in the heat pipe, and L:

$$k_{eff} = \frac{\frac{\alpha(\bar{T}_L)}{2-\alpha(\bar{T}_L)}\sqrt{\frac{R}{2\pi M\bar{T}_L}}\rho_g(\bar{T}_L)\left(\frac{h_{fg}(\bar{T}_L)}{R\bar{T}_L} - \frac{1}{2}\right)}{1 + \frac{\alpha(\bar{T}_L)}{2-\alpha(\bar{T}_L)}\sqrt{\frac{R\bar{T}_L}{2\pi M}}\frac{L\rho_{NCG}}{\rho_{tot}D_{AB}}} h_{fg}L, \tag{19}$$

where D_{AB} is the binary diffusion coefficient. Eq. (19) indicates that in the absence of NCG, i.e., $\rho_{NCG} = 0$, k_{eff} will increase linearly with L. If the NCG is not fully evacuated from the heat pipe, Eq. (19) predicts that k_{eff} will first increase with L and then reach a maximum value given by Eq. (20) in the limit of large L.

$$k_{eff} = \frac{\rho_g}{\bar{T}_L}\left(\frac{h_{fg}}{R\bar{T}_L} - \frac{1}{2}\right)\frac{\rho_{tot}D_{AB}}{\rho_{NCG}}h_{fg}. \tag{20}$$

Eq. (20) indicates that the maximum k_{eff} that can be achieved by a heat pipe is inversely proportional to the density of NCG.

To clearly demonstrate the predictions from Eq. (19), we consider the working fluid in the heat pipe is water and the NCG is air. If the average temperature $\bar{T}_L$ in the heat pipe is 300 K, we use the following experimental data [34,35] of water properties in Eq. (19): (i) saturated vapor density $\rho_g = 0.00142\ mol/L$, (ii) latent heat $h_{fg} = 43.9\ kJ/mol$, (iii) the binary diffusion coefficient of water-air gas mixture [41]:

$$D_{H_2O-air} = 1.87 \times 10^{-10}\frac{T^{2.072}}{P} m^2/s, \tag{21}$$

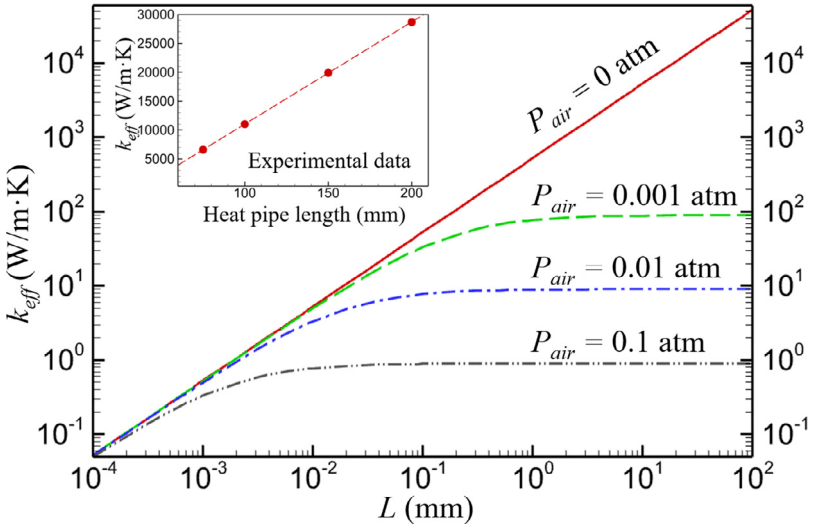

Fig. 8. The variation of k_{eff} with the separation L between evaporating and condensing liquid surfaces in a planar heat pipe predicted by Eq. (19). The working fluid and the non-condensable gas in the heat pipe is water and air, respectively and the average fluid temperature is 300 K. The inset shows the experimental data from Ref. [42].

where the unit of P of the gas mixture is atm. Additionally, we set the MAC of water at 300 K to 1.0 based on our MD simulation result. The ρ_{NCG} (i.e., air density in this case) in Eq. (19) is determined from the air pressure P_{air} in the heat pipe and the ideal gas equation. Figure 8 shows that when air is completely evacuated from the heat pipe, k_{eff} increases linearly with the separation L between evaporating and condensing liquid surfaces, and k_{eff} reaches 5×10^4 $W/m{\cdot}K$ if $L = 100$ mm. This theoretical prediction agrees qualitatively with k_{eff} of a copper heat pipe measured in the recent experiment [42]. As shown in the inset of Fig. 8, the k_{eff} of the copper heat pipe with water as the working fluid increases linearly with heat pipe length, and k_{eff} achieved $\sim 10^4$ $W/m{\cdot}K$ at 100 mm heat pipe length [42].

Note k_{eff} predicted from our theoretical model (i.e., Eq. (19)) is the k_{eff} between the evaporating and condensing liquid surfaces in the heat pipe shown in Fig. 1, while the k_{eff} measured in the experiment is the k_{eff} of the entire heat pipe. The total thermal resistance in a heat pipe includes not only the resistance (R_{ec}) between evaporating and condensing liquid surfaces (i.e., the one studied in our theoretical model), but also the conduction resistance in thin liquid layers (R_L) in the evaporator and condenser of the heat pipe [43] and the conduction resistance in solid walls (R_W) of the heat pipe [44,45]. R_{ec} is the inverse of thermal conductance given by Eq. (16), which is independent of the pipe length when air is completely evacuated from the heat pipe. Using water properties at 300 K, we find from Eq. (16) that $R_{ec} = 1.9 \times 10^{-6}$ $m^2{\cdot}K/W$ which is equivalent to R_L in a 1.2-μm-thick water layer and R_W in a 0.76-mm-thick copper plate. The wick liquid structure in copper heat pipes is often in $\sim$ 10 μm scale [44,45]. Hence, the total thermal resistance in a heat pipe is considerably larger than the resistance (R_{ec}) between evaporating and condensing liquid surfaces. As a result, the k_{eff} of the entire heat pipe is smaller than that calculated by Eq. (19) (i.e., the k_{eff} between the evaporating and condensing liquid surfaces).

If air is not completely evacuated from the heat pipe, Fig. 8 shows k_{eff} eventually reaches a plateau rather than increasing linearly at large L. In this case, the maximum k_{eff} is inversely proportional to P_{air} or ρ_{air} according to Eq. (20). For the specific case shown in Fig. 8, if the partial pressure of air in the heat pipe is 10^{-3} atm, k_{eff} saturates when L reaches $\sim$ 1 mm and the maximum k_{eff} that can reach in the limit of large L is 100 $W/m{\cdot}K$. To achieve k_{eff} =10^4 $W/m{\cdot}K$ in the limit of large L, Eq. (20) suggests that one would need to reduce the air pressure in the heat pipe to below 10^{-5} atm (1 Pa).

6. Conclusions

Using MD simulations, we show Schrage equation is accurate in the prediction of water evaporation and condensation rates in air. Using Schrage equation and Stefan's law, we derive an analytical expression for the effective thermal conductivity between the evaporating and condensing liquid surfaces in a planar heat pipe containing a non-condensable gas. The analytical model shows the effective thermal conductivity will increase linearly with the separation between evaporating and condensing liquid surfaces in the absence of a non-condensable gas. However, if a non-condensable gas is present in the heat pipe, the effective thermal conductivity will reach a plateau at long heat pipe length. The maximum effective thermal conductivity is inversely proportional to the density of the non-condensable gas in the heat pipe.

Since Schrage equation gives accurate predictions of evaporation and condensation rates at a water-air interface, it can be used to formulate appropriate boundary conditions [18] at the water-air interface for continuum modeling of water evaporation and condensation in air [46,47].

Declaration of Competing Interest

The authors claim no conflict of interest.

Acknowledgement

This work was supported by NSF CBET Thermal Transport Processes Program under Grant No. 1911433. P. K. was supported by the Office of Naval Research Thermal Science Program, Award No. N00014-17-1-2767. Additionally, we would like to thank the eXtreme Science and Engineering Discovery Environment (XSEDE) for providing us supercomputer resources for MD simulations.

Justification of significance

Water evaporation/condensation in air is a process of great importance to a variety of natural phenomena and engineering applications. Although recent experimental and molecular dynamics (MD) studies suggest that Schrage equation predicts evaporation and condensation rates of water in the absence of a non-condensable gas with good accuracy, it is not clear whether Schrage equation is still accurate or even valid for quantifying water evaporation and condensation rates in air. In this work, we use MD simulations to show that the evaporation and condensation fluxes of water in the presence of air are still in a good agreement with the predictions from Schrage equation. Based on Schrage equation, we further derive an analytical expression for the effective thermal conductivity of a planar heat pipe. The analytical prediction of the dependence of effective thermal conductivity on heat pipe length and density of non-condensable gas is corroborated by our MD simulation results and recent experimental data.

References

[1] N. Kakitsuba, Dynamic Changes in Sweat Rates and Evaporation Rates through Clothing during Hot Exposure, J. Therm. Biol. 29 (2004) 739–742.
[2] M. Fu, T. Yu, H. Zhang, E. Arens, W. Weng, H. Yuan, A Model of Heat and Moisture Transfer through Clothing Integrated with the UC Berkeley Comfort Model, Build. Environ. 80 (2014) 96–104.
[3] O. Denmead, F. Dunin, R. Leuning, M. Raupach, Measuring and Modelling Soil Evaporation in Wheat Crops, Phys. Chem. Earth 21 (1996) 97–100 1956-1998.
[4] H.A. Loaiciga, J.B. Valdes, R. Vogel, J. Garvey, H. Schwarz, Global Warming and the Hydrologic Cycle, J. Hydrol. 174 (1996) 83–127.
[5] Z. Lu, T.R. Salamon, S. Narayanan, K.R. Bagnall, D.F. Hanks, D.S. Antao, B. Barabadi, J. Sircar, M.E. Simon, E.N. Wang, Design and Modeling of Membrane-Based Evaporative Cooling Devices for Thermal Management of High Heat Fluxes, IEEE Trans. Compon. Packag. Technol. 6 (2016) 1056–1065.
[6] T. Humplik, J. Lee, S. O'Hern, B. Fellman, M. Baig, S. Hassan, M. Atieh, F. Rahman, T. Laoui, R. Karnik, Nanostructured materials for water desalination, Nanotechnology 22 (2011) 292001.
[7] K. Sefiane, On the Formation of Regular Patterns from Drying Droplets and Their Potential Use for Bio-Medical Applications, J. Bionic Eng. 7 (2010) S82–S93.
[8] A.H. Persad, C.A. Ward, Expressions for the evaporation and condensation in the Hertz-Knudsen relation, Chem. Rev. 116 (2016) 7727.
[9] H. Hertz, Ueber die Verdunstung der Flüssigkeiten, insbesondere des Quecksilbers, im luftleeren Raume, Ann. Phys. 253 (1882) 177.
[10] M. Knudsen, Kinetic Theory of Gases, 1950 3rd ed. (London Methuene: London.
[11] R.W. Schrage, A Theoretical Study of Interphase Mass Transfer, Columbia University Press, New York, 1953.
[12] V.P. Carey, Liquid–Vapor Phase-Change Phenomena (Hemisphere, Publishing House, New York, 1992.
[13] Z. Lu, I. Kinefuchi, K.L. Wilke, G. Vaartstra, E.N. Wang, A unified relationship for evaporation kinetics at low Mach numbers, Nat. Commun. 10 (2019) 2368.
[14] A. Chandra, P. Keblinski, Investigating the validity of Schrage relationships for water using molecular dynamics simulations, J. Chem. Phys. 153 (2020) 124505.
[15] Z. Liang, T. Biben, P. Keblinski, Molecular simulation of steady-state evaporation and condensation: validity of the Schrage relationships, Int. J. Heat Mass Transfer 114 (2017) 105.
[16] Z. Liang, P. Keblinski, Molecular simulation of steady-state evaporation and condensation in the presence of a non-condensable gas, J. Chem. Phys. 148 (2018) 064708.

[17] Z. Liang, A. Chandra, E. Bird, P. Keblinski, A molecular dynamics study of transient evaporation and condensation, Int. J. Heat Mass Transfer 149 (2020) 119152.
[18] J. Gonzalez, J. Ortega, Z. Liang, Prediction of thermal conductance at liquid-gas interfaces using molecular dynamics simulations, Int. J. Heat Mass Transfer 126 (2018) 1183.
[19] E. Bird, J. Gutierrez Plascencia, Z. Liang, Thermal transport across the interface between liquid n-dodecane and its own vapor: A molecular dynamics study, J. Chem. Phys. 152 (2020) 184701.
[20] A. Rokoni, Y. Sun, Probing the temperature profile across a liquid-vapor interface upon phase change, J. Chem. Phys. 153 (2020) 144706.
[21] E. Bird, Z. Liang, Transport phenomena in the Knudsen layer near an evaporating surface, Phys. Rev. E 100 (2019) 043108.
[22] E. Bird, Z. Liang, Maximum evaporation flux of molecular fluids from a planar liquid surface, Phys. Rev. E 102 (2020) 043102.
[23] H.J.C. Berendsen, J.R. Grigera, T.P. Straatsma, The Missing Term in Effective Pair Potentials, J. Phys. Chem. 91 (1987) 6269.
[24] D. Wolf, P. Keblinski, S.R. Phillpot, J. Eggebrecht, Exact Method for the Simulation of Coulombic Systems by Spherically Truncated, Pairwise r-1 Summation, J. Chem. Phys. 110 (1999) 8254.
[25] F.N. Mendoza, J. López-Lemus, G.A. Chapela, J. Alejandre, The Wolf Method Applied to the Liquid-Vapor Interface of Water, J. Chem. Phys. 129 (2008) 024706.
[26] C. Kriebel, A. Müller, M. Mecke, J. Winkelmann, J. Fischer, Prediction of Thermodynamic Properties for Fluid Nitrogen with Molecular Dynamics Simulations, Int. J. Thermophys. 17 (1996) 1349.
[27] V.R. Cervellera, M. Alberti, F. Huarte-Larranaga, A molecular dynamics simulation of air adsorption in single-walled carbon nanotube bundles, Int. J. Quant. Chem. 108 (2008) 1714.
[28] M.P. Allen, D.J. Tildesley, Computer Simulation of Liquids, Clarendon Press, Oxford, 2000.
[29] E. Bird, E. Smith, Z. Liang, Coalescence dynamics of bulk nanobubbles in water: a molecular dynamics study coupled with theoretical analysis, Phys. Rev. Fluids (2021) In press.
[30] S.M. Foiles, M.I. Baskes, M.S. Daw, Embedded-atom-method functions for the fcc metals Cu, Ag, Au, Ni, Pd, Pt, and their alloys, Phys. Rev. B 33 (1986) 7983.
[31] A.K. Rappe, C.J. Casewit, K.S. Colwell, W.A. Goddard, W.M. Skiff, UFF, a full periodic table force field for molecular mechanics and molecular dynamics simulations, J. Am. Chem. Soc. 114 (1992) 10024.
[32] I.P. Omelyan, Algorithm for numerical integration of the rigid-body equations of motion, Phys. Rev. E 58 (1998) 1169.
[33] H.J.C. Berendsen, J.P.M. Postma, W.F. Van Gunsteren, A. Di Nola, J.R. Haak, Molecular dynamics with coupling to an external bath, J. Chem. Phys. 81 (1984) 3684.
[34] E. W. Lemmon, M. O. McLinden and D. G. Friend, "Thermophysical Properties of Fluid Systems" in NIST Chemistry WebBook, NIST Standard Reference Database Number 69, Eds.
[35] P.J. Linstrom, W.G. Mallard, National Institute of Standards and Technology, 2021, p. 20899. Gaithersburg MDretrieved August 2.
[36] K. Wark, in: Generalized Thermodynamic Relationships. Thermodynamics, 5th ed., McGraw-Hill, New York, 1988, p. 509.
[37] S. Chandrasekhar, Stochastic Problems in Physics and Astronomy, Rev. Mod. Phys. 15 (1943) 20.
[38] F.O. Goodman, H.Y. Wachman, in: Dynamics of Gas-Surface Scattering, Academic Press, New York, 1976, pp. 23–31.
[39] T. Tsuruta, G. Nagayama, Molecular dynamics studies on the condensation coefficient of water, J. Phys. Chem. B 108 (2004) 1736.
[40] Y.A. Cengel, A.J. Ghajar, in: *Heat and Mass Transfer, Fundamentals & Applications*, 5th Edition in SI Units, McGraw Hill Education, 2014, pp. 864–866.
[41] T.R. Marrero, E.A. Mason, Gaseous Diffusion coefficients, J. Phys. Chem. Ref. Data 1 (1972) 3.
[42] G. Meyer, "Design considerations when using heat pipes", Electronics Cooling, September 2016, pp. 34-39.
[43] X. Wang, Y. Li, J.A. Malen, A.J.H. McGaughey, Assessing the impact of disjoining pressure on thin-film evaporation with atomistic simulation and kinetic theory, Appl. Phys. Lett. 116 (2020) 213701.
[43] G. P. Peterson, "An introduction to Heat pipes – Modeling, Testing and Applications", New York: John Wiley and sons, 1994.
[45] A.B. Solomon, M. Sekar, S.H. Yang, Analytical expression for thermal conductivity of heat pipe, Appl. Therm. Eng. 100 (2016) 462.
[46] A. Dehbi, F. Janasz, B. Bell, Prediction of steam condensation in the presence of noncondensable gases using a CFD-based approach, Nucl. Eng. Des. 258 (2013) 199.
[47] H. Bian, Z. Sun, N. Zhang, Z. Meng, M. Ding, A new modified diffusion boundary layer steam condensation model in the presence of air under natural convection conditions, Int. J. Therm. Sci. 145 (2019) 105948.